Experimental Techniques (2021) 45:445–456
https://doi.org/10.1007/s40799-020-00411-7

RESEARCH PAPER

Estimation and Experimental Validation of Mean-Field Homogenised Effective Properties of Composite

A. Sharma[1] · V. Rastogi[1] · A.K. Agrawal[1]

Received: 27 December 2019 / Accepted: 26 October 2020 / Published online: 23 November 2020

Abstract

For composite materials, the system response changes abruptly with a change in the properties of the material. Therefore, attaining significant knowledge about the effect of the material composition on the material properties is crucial. The researchers are looking for new computational methods which can predict these alterations so that the effort in experimental testing can be reduced. In this direction, this paper presents a robust and novel methodology of validating the estimation of the composite's effective through a multi-scale approach by a set of standardized experimentation. These effective properties are estimated through the mean-field homogenization technique whose parameters are driven from the image analysis of Scanning Electron Microscopy (SEM) images. The predicted results are validated with the results obtained by the experimentation as per ASTM E1876 standard. The estimated error between the predicted properties and the experimental values increased with the increase of alumina particle fraction in the matrix. The mean-field homogenization lags behind the experiments for the parameters defined by the image analysis method than the experimental results. The upper bounds of the mean-field homogenization can be used for the composites with higher reinforcement volume fraction.

Keywords Multi-scale analysis · Mean-field homogenization · Image analysis method · ASTM E1876 · Impact hammer test

Introduction

With the advent of composite materials, industries have started focusing on the use of lighter weight materials with the same mechanical properties. Metal matrix composites have the edge over the parent metals for rotor applications, as it has a higher specific modulus, tensile strength and other mechanical properties. Aluminium /alumina MMCs have shown prominent growth in the composite material market because of their compatibility to the rotor systems. [1–3]. Many manufacturers such as Duralcan, G.K.N., Toyota, GM and Nissan have used MMC materials to develop various components with both static and dynamic applications [4].

Metal matrix composites can be manufactured by various methods from liquid and semi solid-state of matrix mixed with solid reinforcement particles. There are various methods such as powder metallurgy, diffusion bonding, infiltration, stir casting and spray forming to manufacture MMC as per requirements. Stir casting is one of the most inexpensive methods which has been used for the fabrication of metal matrix composites. For complicated and extensive size design of metal matrix composites, stir casting is very convenient and useful [5].

A computation tool that provides results validated by experimental or real-time results saves a lot of time and energy for industries. Researchers seek for more tools that can provide accurate and reliable results for metal matrix composites properties. Multi-scale computation of composites is a two-phase process, where the effective macroscopic properties are derived through micro-mechanics. Analysis of composites with discrete reinforcements with random orientation has been found in archival literature [6–9]. There are various approaches through which these effective properties can be predicted efficiently [10]. For composites with a low volume fraction of inclusions, Eshelby's method [11] with a dilute scheme can be used to evaluate the effective properties. For composites with a higher volume fraction of inclusions, aggregate model [12, 13] can be used, which utilizes the known properties of constituents. Mori-Tanaka [14] have proposed a theory by assuming that the average strain in the inclusion is

✉ A. Sharma
anujsharma_phd2k16@dtu.ac.in

[1] Department of Mechanical, Production, Industrial and Automobile Engineering, Delhi Technological University, Delhi 110042, India

related to the average strain in the matrix by a fourth-order tensor. The relation between the uniform strains in the inclusion in the matrix is provided by this fourth-order tensor. It was further extended by Benveniste [15] to investigate the stress and strain concentration tensors along with the overall elastic modulus of composites. This mean-field homogenization theory has been adopted by various researches [16–20] to determine the effective properties such as modulus, density and thermal expansion and is used in this work.

Significant increase of tensile strength, yield strength and hardness on the addition of alumina particles in the aluminium matrix is validated experimentally in archival literature [21–23]. Properties such as young's modulus, poisson's ratio and shear modulus are computationally derived successfully by various researchers. However, experimental validation of these effective properties with standard practice and technique is equally important. These properties can be experimentally determined by impact hammer test based on ASTM E1876 standard [24].

Recently, *Praveen* et al. [25] performed an impact hammer test based on ASTM E1876 to evaluate the dynamic elastic properties of composites at ambient temperatures. However, the comparison of multi-scale computation of the effective properties and the respective experimental results have not been explored in detail. Daramola et al. [26] compared the mean-field homogenization technique with the experiment and estimated an error of 4.2% between the predicted and experimental values. However, the microscopic parameters such as volume fraction were assumed to be same as the fraction of fibres added during manufacturing. For metal matrix composites fabricated by stir casting method, there is much difference between the added alumina particles and the particles mixed with the matrix. Therefore, a unified and novel approach is adopted in this paper, where the effective properties of the composite are derived computationally using parameters derived through an image analysis method. Moreover, these computationally driven values are compared with the experimental results as per ASTM E1876 standard, evaluated by the impact hammer test.

Material and Method

The composite shaft samples (800 mm length and 22 mm diameter) are fabricated using a stir casting process, as shown in Fig. 1. The aluminium 6061 metal matrix is mixed through stirring with a different weight percentage of alumina (0 wt.%, 6 wt.% and 12 wt.% of alumina) supplied by Loba Chemie Pvt. Ltd. In order to increase the wettability of the alumina particles in the aluminium matrix, the alumina particles were preheated, and magnesium was added during the stir casting process. Magnesium forms an interface of MgO and $MgAl_2O_4$ between the alumina and aluminium, resulting in better wettability and strong bonding [27]. As shown in Fig. 2, the bonding between the reinforcement and the aluminium matrix is strong for both dispersed and agglomerated particles. The Scanning Electron Microscopy (SEM) images are taken for these samples, and then these images are analyzed through an image analysis method. The average aspect ratio and average volume fraction are determined through image analysis. These parameters are used to predict the effective properties of the composite through Mori-Tanaka mean-field homogenization. These properties are then compared with the experimental response of the composite specimen.

Estimation of Effective Mechanical Properties through Mean-Field Homogenization by Using Parameters Extracted through Image Processing

Cubic samples of 5 mm length, 5 mm width and 5 mm height were processed by EDM wire cutting and Scanning Electron Microscopy (SEM) micrographs at the magnification of 500X

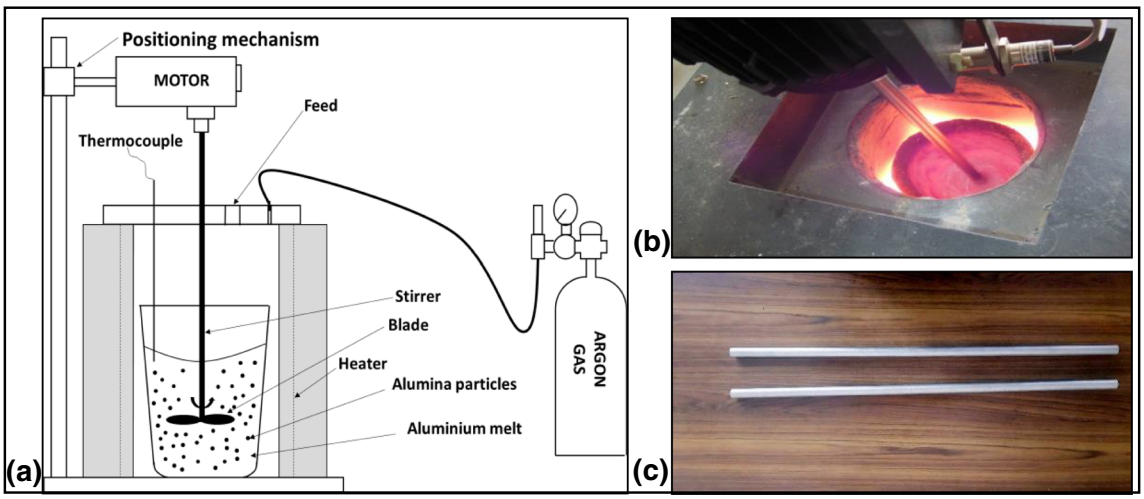

Fig. 1 (**a**) Stir casting set up (**b**) Vortex creation by a four-blade stirrer (**c**) Stir casted 800 x 22 mm shaft

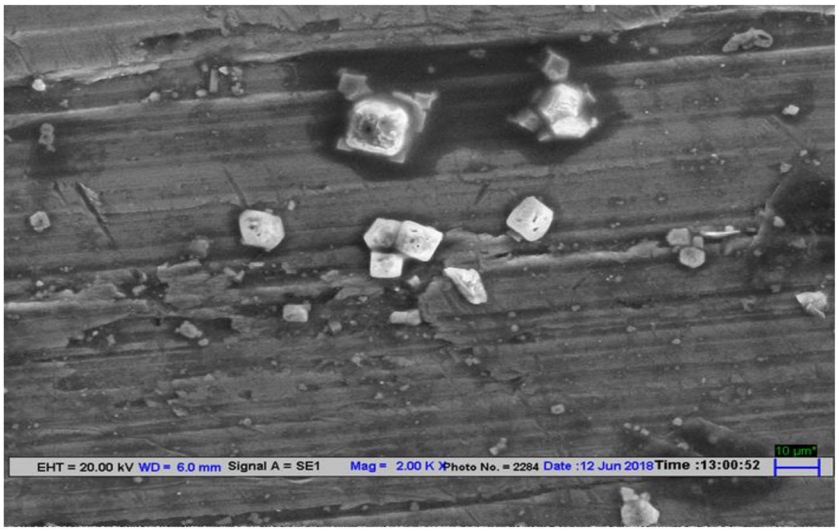

Fig. 2 2000X image showing strong bond between alumina particles and aluminium matrix

and 1000X were obtained using a Zeiss EVO 50 machine. Morphology of the micrographs depicts uniform distribution of reinforcements in the aluminium matrix. For each composition, three samples were scanned, and the fraction and size of alumina particles were evaluated by image processing and averaged for the computation of effective properties.

The open-source image processing software ImageJ was used to generate binary images of the composites with ellipsoid form, assumed for homogenization of properties. SEM micrographs were converted to binary images by using threshold of 61 foreground pixels and 255 background pixels. This transformed the different luminous pixels into white/black bifurcating with respect to the threshold values. At this value of threshold, particles were easily differentiated from the matrix material. Parameters such as the size of the reinforcement, aspect ratio and volume percentage for the composite were derived from the image analysis, as shown in Fig. 3. These parameters were incorporated in the mean-field homogenization of the metal matrix composite material where a Representative Volume Element (RVE) is assumed to be the building block of the macroscopic structure.

RVE is a statistical representation that connects microscopic structure and constituents with the macroscopic properties of composite materials. Therefore, the size of the RVE should

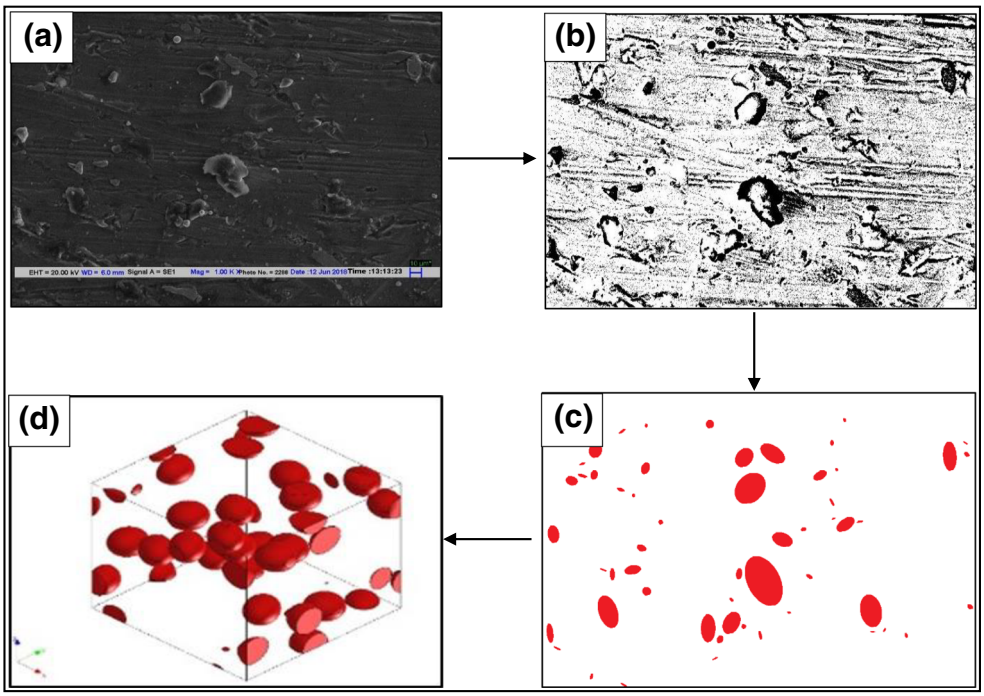

Fig. 3 Conversion of an SEM image into an RVE (**a**) SEM Image of a composite sample (**b**) Cropped SEM image converted into a binary image (**c**) Particle analysation of the binary image (**d**) RVE with mean aspect ratio, size and volume fraction

be such, that it is aptly smaller than the macroscopic structural dimensions and simultaneously large enough to contain an ample amount of information on the microstructure [28, 29].

Digimat is a composite modelling platform which has been used for the generation of RVEs with standard size and threshold. It consists of a Digimat-FE tool, which generates realistic RVEs with the finite element method by using the RVE generation algorithm. This algorithm is based on Random sequential adsorption (RSA) technique which randomizes the orientation of the particles [30]. Particles position themselves in random directions sequentially, and each particle blocks nearby locations from being occupied by another particle, therefore avoiding coagulation. This platform has been used for the development of RVEs in many types of researches. RVEs with randomly distributed spherical inclusions [31, 32], perfectly aligned fibres [33] or random fibre distributions by using a fibre randomization algorithm [34] are generated by using this technique. These RVEs can be exported as standard CAD formats. The effective properties of these RVEs were calculated and have been used for further analysis.

For mean-field homogenization, Mori-Tanaka method [14] has been adopted to determine the effective Young's modulus of the composite material. Therefore, it assumed that the metal matrix composite is comprised of N number of phases. Matrix phase is denoted by subscript m, and there are remaining N-1 inclusion phases in the control volume. The volume fractions of the matrix and the i_{th} inclusion are denoted by ϑ_m and ϑ_i. Similarly, stiffnesses of the matrix and the i_{th} inclusion are denoted by K_m and K_i. These stiffness quantities are generally represented as elasticity tensors of fourth-order which possess specific symmetrical properties. The overall elastic stiffness of the composite [35] is defined in Eq. (1).

$$\bar{\bar{K}}_{av} = \left(\vartheta_m * K_m + \sum_{i=1}^{N-1} \vartheta_i \langle K_i * D_i^{dil} \rangle\right) + \left(\vartheta_m * \boldsymbol{I} + \sum_{i=1}^{N-1} \vartheta_i \langle D_i^{dil} \rangle\right)^{-1} \tag{1}$$

Where $\boldsymbol{I}$ is the identity tensor and the dilute strain concentration factor D_i^{dil} is generally expressed in Eq. (2).

$$D_i^{dil} = \left[\boldsymbol{I} + S_i\, K_m^{-1}(K_i - K_m)\right]^{-1} \tag{2}$$

Here S_i is the Eshelby tensor [6] for the spheroidal inclusion in the infinite matrix.

Since the alumina particles are randomly oriented, orientation averaging has to be taken into account. Therefore, the terms in the angle parentheses ⟨⟩ denote the averaged value of the parameters over all possible orientations. This orientationally averaged tensor is a fourth-order tensor in the 3D space [35] and can be expressed as in Eq. (3).

$$\langle T_{klmn} \rangle = \frac{1}{2\pi} \int_0^{2\pi} \int_0^{2\pi} T_{klmn}(\alpha, \beta) sin\beta \, d\alpha \, d\beta \tag{3}$$

where α, β are the generalized angular orientations. For the randomization, the local coordinates should be transformed to the global coordinates. For overall random transformation, the matrix may be expressed as sown in Eq. (4).

$$a_{kl} = \begin{bmatrix} \cos\alpha & \cos\beta \sin\alpha & \sin\beta \sin\alpha \\ -\sin\alpha & \cos\beta \cos\alpha & \sin\beta \cos\alpha \\ 0 & -\sin\beta & \cos\beta \end{bmatrix} \tag{4}$$

Moreover, the transformation may be written, as shown in Eq. (5).

$$T_{klmn}(\alpha, \beta) = a_{ko} a_{lp} a_{mq} a_{nr}\, T'_{opqr} \tag{5}$$

The effective Young's Modulus(E_{efv}) [35] can be now calculated by the general equation (Eq. (6)) with shear modulus and bulk modulus.

$$E_{efv} = E_m * \frac{\kappa_{efv} * \mu_{efv}(3\kappa_m + \mu_m)}{3k_{efv} * \kappa_m + \mu_{efv} * \mu_m} \tag{6}$$

Effective Shear modulus can be derived using Eq. (7).

$$\frac{\kappa_{efv}}{\kappa_m} = \frac{1}{1 + z\, p} \tag{7}$$

Effective Bulk modulus can be derived using Eq. (8).

$$\frac{\mu_{efv}}{\mu_m} = \frac{1}{1 + z\, q} \tag{8}$$

Where E_{efv} is the effective Young's modulus, E_m is Young's modulus of the matrix, κ_{efv} and μ_{efv} are the effective bulk and shear moduli of the composite, z is the volume concentration/fraction, κ_m and μ_m are the bulk and shear modulus of the matrix. Also, p and q are the explicit expressions, and these expressions and details of the expression can be seen in Tandon and Weng [36] for spheroidal inclusions for detailed reference.

Also, effective density can be easily calculated through the rule of the mixture, as shown in Eq. (9).

$$\rho_{efv} = \rho_m \vartheta_m + \rho_i \vartheta_i \tag{9}$$

Where ρ_{efv} is the effective density, ρ_m and ϑ_m are the density and volume fraction of matrix and ρ_i and ϑ_i are the density and volume fraction of inclusions.

Experimental Evaluation of Elastic Properties

For the experimental validation of the estimated/predicted properties of the composites, ASTM E1876 impact hammer vibration analysis was employed. The analysis is performed on a standard experiment setup which conforms the prerequisites for the ASTM E1876 standard, as shown in Fig. 4.

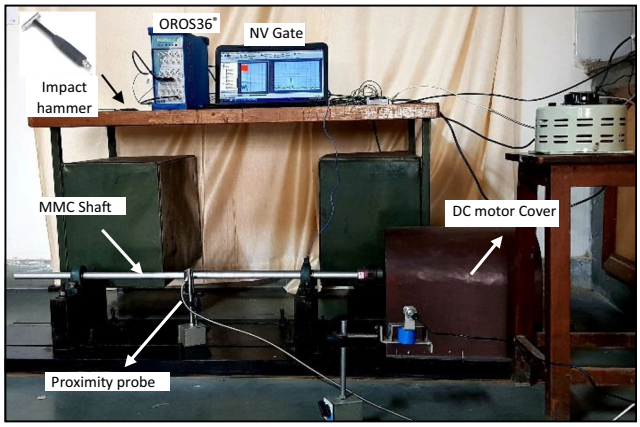

Fig. 4 Experimental set up for impact hammer test

The inductive proximity sensor (LJ12A3–4-Z /BY) having a sensitivity of 1000 V/m and a detection range of 4000 μm is used. The test specimens are energized through a force transducer with a plastic tip. Impact Hammer (Model: - PCB-086C03) with sensitivity 2250 μ(V)/(N) and range 4440 N is used for transient excitation. The response from the transducers is collected and analyzed by using a 32 channel, vibration analyzer OROS36®. The channels of these analyzers are handled in real-time: FFT, 1/3rd Octave. The fundamental natural frequencies of the specimen are observed from the peaks of the frequency response function obtained by using NV Gate® (version 10.1.1) interface.

The prime objective of the experimentation was to extract the values of natural frequencies for the first two bending (flexural) modes of the shaft. A range of 0–600 Hz was targeted as per the dimensions for experimental analysis to confirm that primarily these modes are excited. For excitation, the plastic tip of suitable hardness was used such that the input spectrum doesn't prominently excite the frequencies beyond the working range. The experimental samples were selected carefully such that the impact force input spectrum excites the required range of frequency at amplitude high enough to avoid noise interceptions. The sampling rate of 2.04 kS/s (kilo samples per second) was chosen, which was much higher than the Nyquist frequency according to the range excited by the input spectrum and the range of observation. This high rate of sampling prevented the problem of leakage and aliasing, and no anti-aliasing filters were required. The motive of the experimentation was also to observe the damping of the material relative to each other. The windowing technique would have altered the peak width and thus, the estimation of damping. Therefore, the time range was taken in such a way that windowing was not required for sample selection. The high resolution of the sampling ensured that the natural frequency is confidently determined by Gaussian peak fitting method. The position of the sensor has to be chosen in such a way that it should detect the first and second mode excitation. At the centre of the shaft, the first mode was highly excited, but the second mode was not excited (Since the antinode of the second mode is at the centre for the simply supported system). Therefore, a non-contact inductive proximity transducer was roved, and a suitable position was chosen where the excitation of first and second peaks was obtained successfully (At a distance of 50 mm from the centre as shown in Fig. 5. At this position, the amplitude of first bending natural frequency peak is the highest followed by second bending natural frequency peak.

The Young's modulus expression for the known fundamental flexural natural frequency is shown in Eq. (10).

$$E = 1.6067\left(\frac{l^3}{d^4}\right)\left(mf_f^2\right)T_1 \tag{10}$$

where E = Young's modulus, l = Length of the specimen, d = diameter of the shaft, m = mass of the shaft, f_f = fundamental

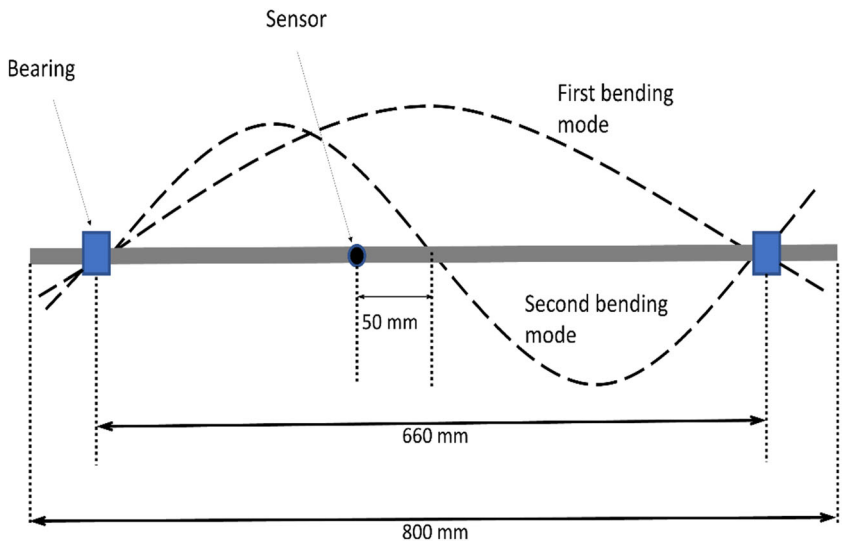

Fig. 5 First and second bending mode with sensor positioning

Table 1 Mean volume fraction, aspect ratio and particle size for various SEM images

Shaft Material		Mean volume fraction			Mean aspect ratio			Mean particle size (μm)		
		S1	S2	S3	S1	S2	S3	S1	S2	S3
Al 6061/6 wt.% Al_2O_3	Max	4.0	4.8	4.7	3.1	2.9	3.1	8.7	8.9	8.8
	Min	2.9	3.4	3.1	2.6	2.6	2.7	7.3	7.2	7.1
	Mean	3.4	4.1	3.8	2.9	2.7	3.0	8.0	8.1	8.1
Al 6061/12 wt.% Al_2O_3	Max	8.3	9.4	9.9	3.4	3.2	3.3	8.9	8.8	9.0
	Min	6.9	7.4	7.9	2.8	2.7	2.9	7.3	7.5	7.4
	Mean	7.3	8.1	9.1	3.2	3.0	3.1	8.3	8.2	8.4

flexural frequency of the shaft and T_1 = correction factor for the fundamental flexural mode to account for finite diameter of the rod, and Poisson's ratio.

Since the aspect ratio (l/d) is higher than 20, the simplified form for T_1 can be used as shown in Eq. (11).

$$T_1 = \left[1 + 4.939\left(\frac{d}{l}\right)^2\right] \tag{11}$$

The expression for Dynamic shear modulus for known fundamental torsion resonant frequency of a cylindrical is shown in Eq. (12).

$$G = 16mf_t^2\left(\frac{l}{\pi d^2}\right) \tag{12}$$

where G = Dynamic shear modulus, l = Length of the specimen, d = diameter of the shaft, m = mass of the shaft, f_t = fundamental torsional frequency of the shaft.

Correspondingly, Poisson's Ratio can be determined using Eq. (13).

$$\mu = \left(\frac{E}{2G}\right) - 1 \tag{13}$$

Where μ is the Poisson's ratio.

Results and Discussion

Since there might be inhomogeneous zones within the sample which lead to interference of the results, measures are taken to avoid these uncertainties. Three samples were taken for each material for SEM analysis. The SEM images were randomly taken for different positions within the sample and all six surfaces of the cuboid sample with 1000x magnifications. For each sample (S1, S2 and S3), maximum, minimum, and mean values of volume fraction, aspect ratio and particle size are taken for various SEM micrographs as shown in Table 1.

The aspect ratio and particle size doesn't vary much for different samples and materials. The mean volume fraction increased for the Al 6061/12 wt.% Al_2O_3 as compared to the Al 6061/6 wt.% Al_2O_3. The variation of the microstructural parameters within the sample were not resulting in interference with the microstructural parameters of different composition. For example, the mean volume fraction ranges from 2.9 to 4.8 for Al 6061/6 wt.% Al_2O_3 and 6.9 to 9 for Al 6061/12 wt.% Al_2O_3. The data is therefore categorical, and we can classify the results for different composition of materials respectively.

The modulus of elasticity is highest for the largest volume fraction, highest aspect ratio and smallest mean particle size and vice versa. Therefore, the overall highest young's modulus can be predicted by taking mean volume fraction as 4.8, aspect ratio as 3.1 and mean particle size as 7.1 μm and vice versa for Al 6061/6 wt.% Al_2O_3. Also, overall highest young's modulus can be predicted by taking mean volume fraction as 9.7, aspect ratio as 3.4 and mean particle size as 9.0 μm and vice versa for Al 6061/12 wt.% Al_2O_3. The consolidated results for the estimated microscopic properties through image analysis and mean-field homogenization are shown in Table 2.

On the addition of 6 wt.% of alumina, the overall mean volume fraction of 3.8% is observed by image analysis of

Table 2 Image analysis overall mean results

Material	Mean volume fraction	Mean aspect ratio	Mean particle size (μm)
Al 6061	–	–	–
6 wt.% Al_2O_3/Al 6061	3.8	2.9	8.1
12 wt.% Al_2O_3/Al 6061	8.166	3.1	8.3

Table 3 Mean-field homogenization results

Engineering constants	Al 6061	6 wt.% Al_2O_3/Al 6061			12 wt.% Al_2O_3/Al 6061		
		Mean	Max	Min	Mean	Max	Min
In-Plane Young's modulus (GPa)	70	73.73	74.84	72.9	78.66	80.1	77.4
Out -Plane Young's modulus (GPa)	70	73.61	74.71	72.78	78.32	79.75	77.06
In-Plane Poisson's ratio	0.328	0.326	0.325	0.326	0.322	0.321	0.323
Transverse Poisson's ratio	0.328	0.326	0.325	0.326	0.322	0.321	0.323
In-Plane shear modulus (GPa)	26.35	27.8	28.21	27.48	29.75	30.29	29.27
Transverse shear modulus (GPa)	26.35	27.76	28.17	27.44	29.2	29.73	28.73
Global Density (Kg/m^3)	2710	2748	2772	2723	2798	2838	2753

SEM images for different samples. The observed volume fraction of alumina in fabricated samples is low as compared to the volume fraction of alumina added during stir casting. The limitation of stir casting method that all alumina particles are not mixed with the matrix is the reason for this deviation. Although stir casting is flexible enough and large-sized samples used for analysis can be easily manufactured through this method. Similarly, for the addition of 12 wt.% of alumina particles, the mean volume fraction of 8.166% is observed. The mean aspect ratio and the average particle size are also in the conformance with the alumina particles manufacturer specification.

The effective Young's Modulus, Poisson's ratio and the shear modulus of in-plane and transverse plane for a particular RVE is estimated through mean-field homogenization as shown in Table 3.

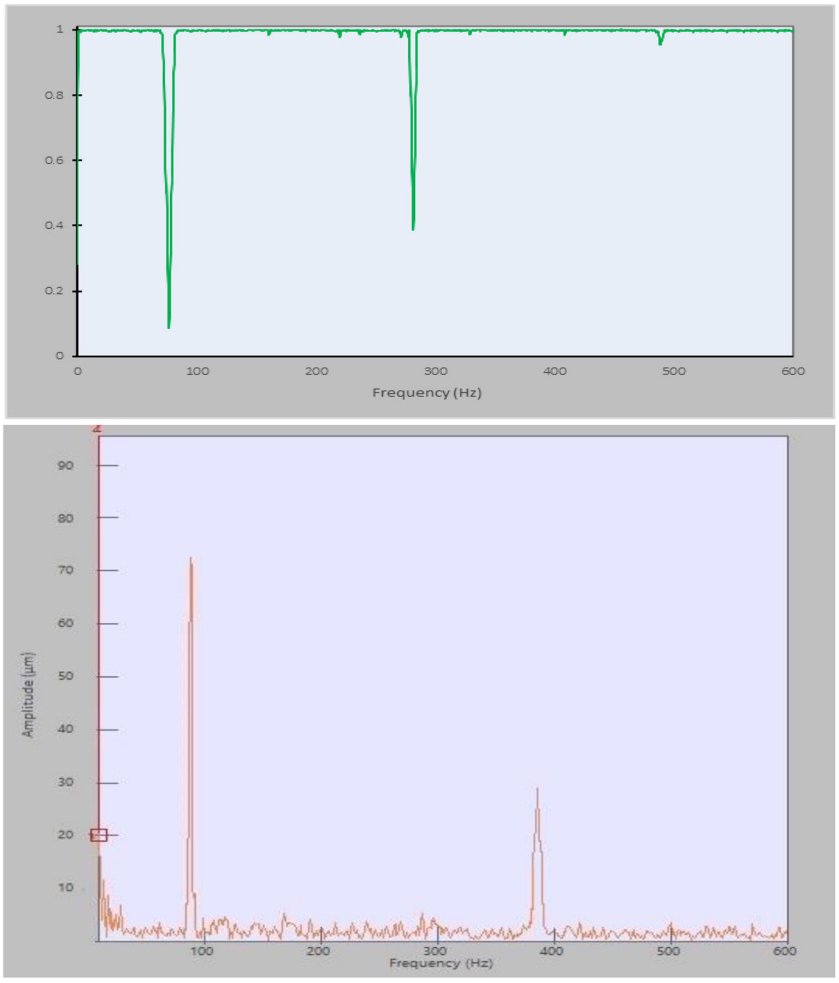

Fig. 6 FRF and coherence for Al6061

The estimated mean In-plane Young's modulus is increased by 5.32%, on the addition of 6 wt.% of alumina due to enhanced dislocation density and precipitation hardening. Since the orientation of the particles is randomized, the value of out of plane Young's modulus is approximately the same as values of In-plane Young's modulus. The global density of the composite is also estimated to be increased by the addition of the particles since the density of the alumina particles is more than the aluminium matrix. The mean In-Plane shear modulus is also increased by 5.5% with transverse shear modulus value approximately similar to the In-plane shear modulus. Moreover, the effective In-plane Young's Modulus is estimated to be increased by 12.37% on addition of 12 wt.% of alumina. The highest value of density and shear modulus is observed for the composite with 12 wt.% of alumina reinforcements.

As shown in Table 3, there is no interference in respective values of Young's modulus, Poisson's ratio and shear modulus for different materials. For example, the minimum value of In-plane young's modulus of 12 wt.% Al_2O_3/Al 6061 is 77.4 GPa, whereas the maximum value of In-plane young's modulus of 6 wt.% Al_2O_3/Al 6061 is 74.84 GPa. So, this data can be classified by the composition of the material.

The strengthening effect of reinforcement is not directionally dependent as in the case of fibre reinforced composites due to the random orientation of particles. By adding 12 wt.% of alumina, In-Plane Young's modulus is increased by 12.37%, but the global density is increased by 3.2%. It implies that the addition of reinforcement improves the specific modulus of the material and therefore improves the modal response of the material. Therefore, impact hammer test is performed to obtain the properties of composites through modal response.

The frequency response function and the coherence for Al6061, Al6061/6 wt.% Al_2O_3 and Al6061/ 12 wt.% Al_2O_3 composite in the impact hammer test is shown in Figs. 6, 7 and 8. The input and output spectrums were coherent for all shafts with the resonance value dropped at anti-nodes. The high coherence between the input and output spectrum, except at the anti-nodes confirms the replicability of the experiments. The high resolution of the frequency spectrum was obtained because of the high sampling rate. The amplitude and the natural frequency were calculated by determining the peak using the Gaussian peak fitting method, and the damping ratio is obtained by the half-power bandwidth method.

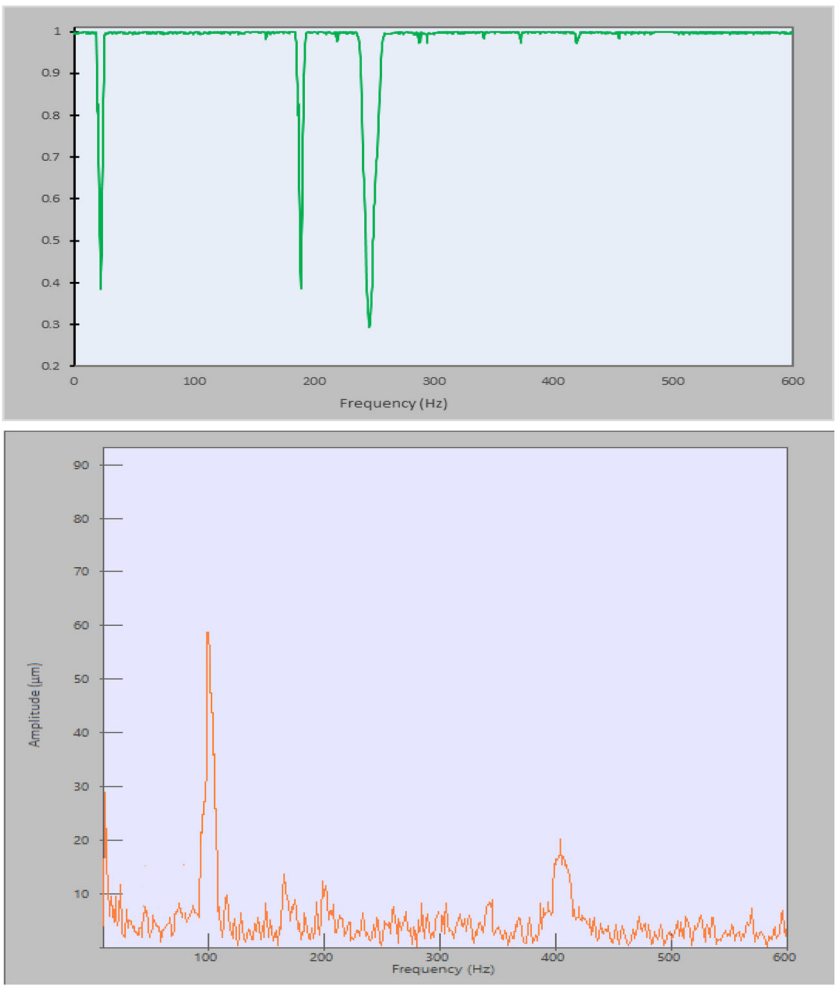

Fig. 7 FRF and coherence for Al6061/ 6 wt. % Al_2O_3

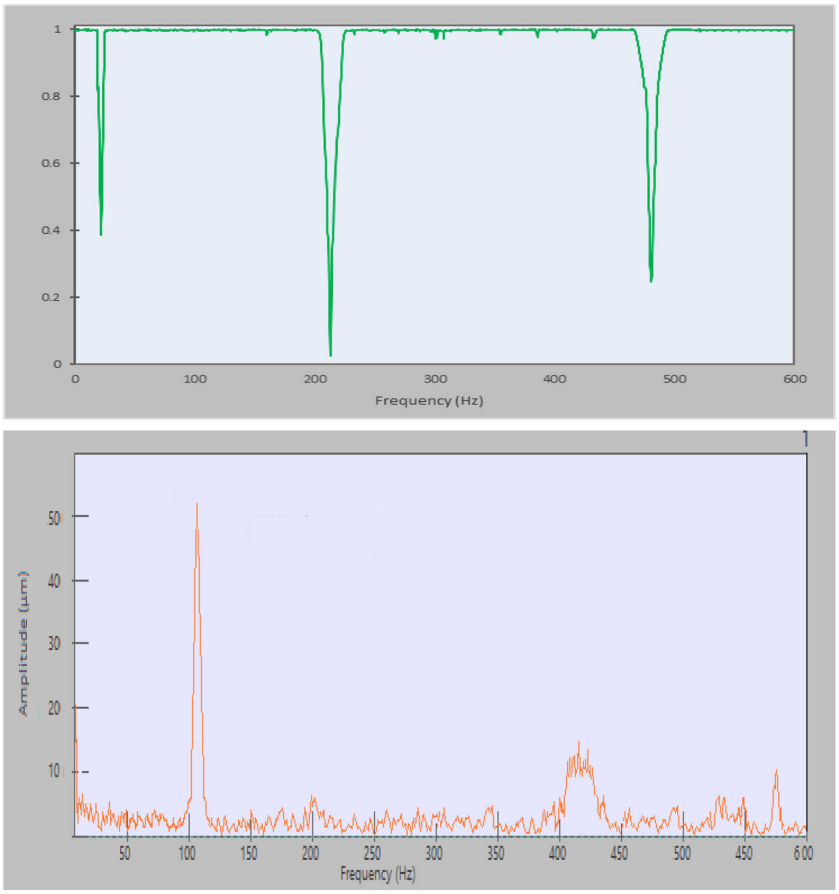

Fig. 8 FRF and coherence for Al6061/ 12 wt. % Al_2O_3

For each shaft with different composition, thirty experiments were taken for the determination of natural frequencies, damping ratio and amplitudes. The mean, standard deviation and range of the natural frequencies for different sets of experimentations are shown in Table 4.

The low standard deviation was obtained for the values of natural frequencies for both first and second mode. Also, the range of natural frequency values for different composition doesn't interfere with each other. The natural frequency increases significantly with the increase of reinforcement particles in the shafts. This is due to the reason that the addition of alumina particles in the Al6061 matrix leads to a substantial improvement in the bending stiffness as compared to the material density. The mean, standard deviation and range of the damping for different sets of experimentations are shown in Table 5.

The higher value of damping was observed for the specimen with higher wt.% of alumina particles in the aluminium matrix. The damping was significantly increased for the second mode of vibration. It suggests that the damping increases with the increase of alumina particles in the aluminium matrix. This is due to the grain refinement and formation of secondary phases which increases elastic strain energy dissipation in the materials.

The mean, standard deviation and range of the amplitude of vibrations for different sets of experimentations are shown in Table 6.

Table 4 Experimental natural frequency mean, standard deviation and range

Shaft Material	Natural frequency (first mode)			Natural frequency (second mode)		
	Mean	Standard deviation	Range	Mean	Standard deviation	Range
Al6061	98.62	0.65	97.6–99.1	388.93	1.92	386.1–391.6
Al 6061/6 wt.% Al_2O_3	101.65	0.72	100.1–102.8	408.43	2.42	406.3–411.7
Al 6061/12 wt.% Al_2O_3	108.91	1.01	107.1–110.7	420.21	3.02	416.2–425.1

Table 5 Experimental damping mean, standard deviation and range

Shaft Material	Damping (first mode)			Damping (second mode)		
	Mean	Standard deviation	Range	Mean	Standard deviation	Range
Al6061	0.0097	0.0001	0.0095–0.0099	0.021	0.0003	0.0207–0.026
Al 6061/6 wt.% Al_2O_3	0.0123	0.0004	0.0119–0.0129	0.0233	0.0005	0.0225–0.0242
Al 6061/12 wt.% Al_2O_3	0.0146	0.0006	0.0137–0.155	0.026	0.0008	0.0252–0.0262

Table 6 Experimental amplitude mean, standard deviation and range

Shaft Material	Amplitude (first mode) (μm)			Amplitude (second mode) (μm)		
	Mean	Standard deviation	Range	Mean	Standard deviation	Range
Al6061	69.1	2.11	67.1–70.9	30.21	2.01	31.2–27.1
Al 6061/6 wt.% Al_2O_3	62.7	2.03	60.7–64.2	21.62	2.42	22.5–19.1
Al 6061/12 wt.% Al_2O_3	52.1	2.81	50.2–54.8	14.29	2.65	12.31–17.01

The amplitude reduced significantly with the increase in alumina particles for both the modes. The range and the standard deviation are well within the limit that is required for the data to be categorical about the composition of the material. This is due to the increase in bending stiffness of the shafts because of the reinforcing effect of the alumina particles in the matrix.

These values are utilized to obtain the value of In-plane Young's modulus, shear modulus and Poisson's ratio experimentally, as per ASTM E1876 standard. The comparison of predicted values obtained through mean-field homogenization and the experimental values obtained is shown in Table 7.

The experimental value of In-plane Young's modulus of Al 6061 is observed to be 2.88% lower than that of initial prediction. This lower value can be attributed to the defects induced during the casting process of aluminium alloy. However, these defects might have prevailed for the case of 6 wt.% Al_2O_3/Al 6061 also, but the experimental In-plane Young's modulus has increased by 1.19% as compared to the predicted value. Similarly, experimental In-plane Young's modulus has increased by 3.75% as compared to the predicted value for the case of 12 wt.% Al_2O_3/Al 6061. From literature [26], it is observed that the addition of 6 wt.% micro-sized kaolinite particle in epoxy polymer matrix composite increased the effective elastic modulus from 3100 MPa to 3107.5 MPa. The mean-field homogenization method predicted the value 4.2% higher than the experimental value. Whereas in the present study, the mean-field homogenization predicted the value 1.19% lower than the experimental values. The reason for predicting a lower value by the homogenization process may be that the actual alumina particle volume fraction is higher than the volume fraction estimated by image analysis.

The range of the experimental and the predicted values for the In-plane Young's modulus is shown in Fig. 9. For Al 6061, the predicted value is the standard value for Young's modulus, and the experiment values are of the cast material. Therefore, the values are lower due to the introduction of some porosity. For, Al 6061/ 6 wt.% Al_2O_3 the experimental range intersects with the predicted value range. For, Al 6061/ 12 wt.% Al_2O_3 the experimental range exceeds the predicted

Table 7 Comparison of Predicted and experimental value

Engineering constants	Al 6061		6 wt.% Al_2O_3/Al 6061		12 wt.% Al_2O_3/Al 6061	
	Predicted	Experimental	Predicted	Experimental	Predicted	Experimental
In-Plane Young's modulus	70 GPa	67.98 GPa	73.73 GPa	74.61 GPa	78.66 GPa	81.61 GPa
In-Plane shear modulus	26.35 GPa	25.55 GPa	27.82 GPa	29.01 GPa	29.75 GPa	30.91 GPa
In-Plane Poisson's ratio	0.328	0.327	0.326	0.323	0.322	0.320

Fig. 9 Comparison of range of predicted and experimental value of In-plane Young's modulus

value range at a few points. Therefore, it can be concluded that the upper bounds of mean-field solutions should be used for the higher reinforcement compositions.

The similar kind of trend is observed for In-plane shear modulus, and the mean-field homogenization analysis does not deviate significantly from the experimental results.

Conclusion

The composite specimens have been successfully fabricated by stir casting method as per ASTM E1876 standards. The microstructure of the composites was taken through SEM and particles average size; aspect ratio and fraction were obtained through image analysis method. The effective properties were then evaluated by mean-field homogenization method by using these parameters. These properties were then evaluated experimentally as per ASTM E1876 standards. Following conclusions can be driven from the analysis in this paper:

- The volume fraction of the alumina particles observed by the image analysis method was significantly less as compared to the added volume fraction during fabrication. It suggests that the volume fraction added initially during fabrication should not be used directly for predicting the effective properties.
- The addition of alumina particles results in the strengthening of composite specimens due to enhanced dislocation density and precipitation hardening.
- The difference between the In-Plane and transverse effective properties is negligible since the strengthening effect of reinforcement is not directionally dependent due to the random orientation of particles.
- The addition of alumina particles in the Al6061 matrix leads to a substantial improvement in the bending stiffness as compared to the material density. Due to this reason, the natural frequency for various modes of vibration increased on the addition of particles.
- Damping ratio also increased on the addition of alumina particles due to the grain refinement and formation of secondary phases.
- The estimated error for the case of 6 wt.% Al_2O_3/Al 6061 is 1.19%, whereas the estimated error for the case of 6 wt.% Al_2O_3/ Al6061 is 3.75% for the mean values.
- The range of mean-field values lags behind the experimental values as the material of high reinforcement composition is used. It can be concluded that the upper bound of mean-field homogenization can be used for the material of high reinforcement composition and can be the future scope of work. However, mean-field homogenization predicts a low higher than experimental value while assuming that all alumina particles added for process are mixed into the matrix.
- Also, samples were taken from the end of the shaft for SEM analysis; this might be the low/high composition area of the shaft during casting. This variation can be addressed in future work.
- The variation of the experimental and the predicted values was such that categorization of the values was possible in reference to the composition of the shaft.

Author's Contribution All authors contributed to the study conception and design. Material preparation, data collection and analysis were performed by Mr. Anuj Sharma, Prof. Vikas Rastogi and Prof. Atul kumar agrawal The first draft of the manuscript was written by Mr. Anuj Sharma and all authors commented on previous versions of the manuscript. All authors read and approved the final manuscript.

Compliance with Ethical Standards

Conflict of Interest The authors declare that they do not have any conflict of interest.

References

1. Chawla N, Shen YL (2001) Mechanical behavior of particle reinforced metal matrix composites. Adv Eng Mater 3(6):357–370. https://doi.org/10.1002/1527-2648(200106)3:6<357::AID-ADEM357>3.0.CO;2-I
2. Rawal S (2001) Metal-matrix composites for space applications. Jom 53(4):14–17. https://doi.org/10.1007/s11837-001-0139-z
3. Sarmasti AB, Yazdanirad M, Nouri Khezrabad M, Karbalaie M (2011) Effect of alumina particle size and thermal condition of casting on microstructure and mechanical properties of stir cast Al-Al2O 3 composites. Mater Sci Technol 27(11):1653–1656. https://doi.org/10.1179/1743284710Y.0000000020
4. Koczak MJ, Khatri SC, Allison JE, Bader MG (1993) Metal-Matrix Composites for Ground Vehicle, Aerospace, and Industrial Applications. Fundamentals of Metal-Matrix Composites, 297–326. https://doi.org/10.1016/b978-0-08-052371-2.50020-1
5. Singh S, Singh I, Dvivedi A Design and development of novel cost-effective casting route for the production of metal matrix composites (MMCs) (2017). Int J Cast Metals Res 6(30):356–364. https://doi.org/10.1080/13640461.2017.1323605

6. Chaturvedi SK, Tzeng GY (1991) Micromechanical modeling of material damping in discontinuous fiber three-phase polymer composites. Compos Eng 1(1):49–60. https://doi.org/10.1016/0961-9526(91)90025-N
7. Guden M, Hall IW (1998) Dynamic properties of metal matrix composites: a comparative study. Mater Sci Eng A 242(1–2): 141–152. https://doi.org/10.1016/s0921-5093(97)00516-9
8. Lesieutre GA, Yarlagadda S, Yoshikawa S, Kurtz SK, Xu QC (1993) Damped structural composite material using resistively-shunted piezoelectric ceramic short fibers. Collect Tech Papers - AIAA/ASME Structures, Structural Dynamics Mater Conf (pt 6): 3238-3243
9. Vaidya UK, Dadzie P-E, Haque A, Mahfuz H, Jeelani S (1997) Nondestructive evaluation and characterization of microfibers modified textile carbon-phenolic and carbon-carbon composites. J Reinf Plast Compos 16(11):968–1001. https://doi.org/10.1177/073168449701601101
10. Mura T (2013) Micromechanics of defects in solids. Mechanics of Elastic and Inelastic Solids. Springer Science & Business Media. https://doi.org/10.1007/978-94-009-3489-4
11. Eshelby JD (1957) The determination of the elastic field of an ellipsoidal inclusion, and related problems. Proc Royal Soc A: Math Phys Eng Sci 241(1226):376–396. https://doi.org/10.1098/rspa.1957.0133
12. Christensen RM, Waals FM (1972) Effective stiffness of randomly oriented fibre composites. J Compos Mater 6(3):518–535. https://doi.org/10.1177/002199837200600307
13. Halpin JC, Jerine K, Whitney JM (1971) The laminate analogy for 2 and 3 dimensional composite materials. J Compos Mater 5(1):36–49. https://doi.org/10.1177/002199837100500104
14. Mori T, Tanaka K (1973) Average stress in matrix and average elastic energy of materials with misfitting inclusions. Acta Metall 21(5):571–574. https://doi.org/10.1016/0001-6160(73)90064-3
15. Benveniste Y (1987) A new approach to the application of Mori-Tanaka's theory in composite materials. Mech Mater 6(2):147–157. https://doi.org/10.1016/0167-6636(87)90005-6
16. Abaimov SG, Trofimov A, Sergeichev IV, Akhatov IS (2019) Multi-step homogenization in the Mori-Tanaka-Benveniste theory. Compos Struct. https://doi.org/10.1016/j.compstruct.2019.03.073
17. Imani SM, Goudarzi AM, Rabiee SM, Dardel M (2018) The modified Mori-Tanaka scheme for the prediction of the effective elastic properties of highly porous ceramics. Ceram Inter 44(14):16489–16497. https://doi.org/10.1016/j.ceramint.2018.06.066
18. Kamarian S, Shakeri M, Yas MH (2016) Natural frequency analysis and optimal design of CNT/fiber/polymer hybrid composite plates using Mori-tanaka approach, GDQ technique, and firefly algorithm. Polym Compos 39(5):1433–1446. https://doi.org/10.1002/pc.24083
19. Tran VP, Brisard S, Guilleminot J, Sab K (2018) Mori–Tanaka estimates of the effective elastic properties of stress-gradient composites. Int J Solids Struct 146:55–68. https://doi.org/10.1016/j.ijsolstr.2018.03.020
20. Sobhaniaragh B, Batra RC, Mansur WJ, Peters FC (2017) Thermal response of ceramic matrix nanocomposite cylindrical shells using Eshelby-Mori-Tanaka homogenization scheme. Compos Part B 118:41–53. https://doi.org/10.1016/j.compositesb.2017.02.032
21. Yılmaz O, Buytoz S (2001) Abrasive wear of Al_2O_3-reinforced Aluminium-based MMCs. Compos Sci Technol 61:2381–2392
22. Kok M (2005) Production and mechanical properties of Al_2O_3 particle-reinforced 2024 Aluminium alloy composites. J Mater Process Technol 161:381–387
23. Suthar J, Patel KM (2018) Processing issues, machining, and applications of aluminium metal matrix composites. Mater Manuf Process 33(5):499–527. https://doi.org/10.1080/10426914.2017.1401713
24. Standard Test Method for Dynamic Young's Modulus, Shear Modulus, and Poisson's Ratio by Impulse Excitation of Vibration. ASTM E1876, ASTM International, United States, 1–17
25. Praveen AP, Rajamohan V, Mathew AT (2019) Material and mechanical characterization of multi-functional carbon nanotube reinforced hybrid composite materials. Exp Tech 43(3):301–314. https://doi.org/10.1007/s40799-019-00316-0
26. Daramola OO, Olajide JL, Adediran AA, Adewuyi BO, Ayodele TT, Desai DA, Sadiku ER (2020) Multiscale analysis and experimental validation of the effective elastic modulus of epoxy-dioctahedral phyllosilicate clay composite. Heliyon 6(6):e04008. https://doi.org/10.1016/j.heliyon.2020.e04008
27. Sangghaleh A, Halali M (2009) Effect of magnesium addition on the wetting of alumina by aluminium. Appl Surf Sci 255:8202–8206. https://doi.org/10.1016/j.apsusc.2009.05.044
28. Bouhfid N, Raji M, Boujmal R, Essabir H, Bensalah M-O, Bouhfid R, Qaiss AeK. (2019) Numerical modeling of hybrid composite materials. Modelling of Damage Processes in Biocomposites, Fibre-Reinforced Composites and Hybrid Composites, 57–101. https://doi.org/10.1016/b978-0-08-102289-4.00005-9
29. Gitman IM, Askes H, Sluys LJ, Valls OL (2004) The concept of representative volume for elastic, hardening and softening materials. International Summer School - IPME conference. XXXII International Summer School - IPME Conference: Advanced Problems in Mechanics. p 1-5
30. Babu KP, Mohite PM, Upadhyay CS (2018) Development of an RVE and its stiffness predictions based on mathematical homogenization theory for short fibre composites. Int J Solids Struct 130-131:80–104. https://doi.org/10.1016/j.ijsolstr.2017.10.011
31. Klusemann B, Svendsen B (2010) Homogenization methods for multi-phase elastic composites: comparisons and benchmarks. Tech Mech 30(4):374–386
32. Yi I, Wiedmaier J, Schmauder S (2015) Modeling and simulation of mechanical properties of nano particle modified polyamide 6. J Mater Sci Chem Eng 3(1):80–87
33. Ogierman W, Kokot G (2016) A study on fiber orientation influence on the mechanical response of a short fiber composite structure. Acta Mech 227(1):173–183
34. Soni G, Singh R, Mitra M, Falzon BG (2014) Modelling matrix damage and fibre matrix interfacial decohesion in composite laminates via a multi-fibre multilayer representative volume element (M2RVE). Int J Solids Struct 51(2):449–461
35. Chang CY, Chang MY, Huang JH (2004) Vibration analysis of rotating composite shafts containing randomly oriented reinforcements. Compos Struct 63(1):21–32
36. Tandon GP, Weng GJ (1986) Average stress in the matrix and effective moduli of randomly oriented composites. Compos Sci Technol 27(2):111–132. https://doi.org/10.1016/0266-3538(86)90067-9